Sea-level constraints on the amplitude and source distribution of Meltwater Pulse 1A

Jean Liu[1], Glenn A. Milne[1]*, Robert E. Kopp[2], Peter U. Clark[3] and Ian Shennan[4]

During the last deglaciation, sea levels rose as ice sheets retreated. This climate transition was punctuated by periods of more intense melting; the largest and most rapid of these—Meltwater Pulse 1A—occurred about 14,500 years ago, with rates of sea-level rise reaching approximately 4 m per century[1-3]. Such rates of rise suggest ice-sheet instability, but the meltwater sources are poorly constrained, thus limiting our understanding of the causes and impacts of the event[4-7]. In particular, geophysical modelling studies constrained by tropical sea-level records[1,8,9] suggest an Antarctic contribution of more than seven metres, whereas most reconstructions[10] from Antarctica indicate no substantial change in ice-sheet volume around the time of Meltwater Pulse 1A. Here we use a glacial isostatic adjustment model to reinterpret tropical sea-level reconstructions from Barbados[2], the Sunda Shelf[3] and Tahiti[1]. According to our results, global mean sea-level rise during Meltwater Pulse 1A was between 8.6 and 14.6 m (95% probability). As for the melt partitioning, we find an allowable contribution from Antarctica of either 4.1 to 10.0 m or 0 to 6.9 m (95% probability), using two recent estimates[11,12] of the contribution from the North American ice sheets. We conclude that with current geologic constraints, the method applied here is unable to support or refute the possibility of a significant Antarctic contribution to Meltwater Pulse 1A.

Using a glacial isostatic adjustment (GIA) sea-level model (see Methods), global sea-level changes for a wide range of ice histories were calculated and then compared to palaeo-sea-level reconstructions (based on indicators such as corals and mangroves, including their uncertainties) to assess whether a given Meltwater Pulse 1A (MWP-1A) source scenario is compatible with the field constraints. We focused on modelling the relative sea-level (rsl) change across MWP-1A to reduce the sensitivity of the analysis to mantle viscosity structure, which is not precisely known. A primary limitation of this approach is that there are only three far-field sites (locations in low latitudes distant from ice sheets) where sea-level records constrain the amplitude of MWP-1A: Barbados, Sunda Shelf and Tahiti. Within this limited data framework, a key aim of this study is to quantify the possible MWP-1A source constraints through a sea-level fingerprinting[8,13] analysis when both data and model uncertainty are taken into consideration.

MWP-1A was first identified at Barbados from reef framework-forming corals with species-dependent depth ranges[14,15]. By assuming that the coral growth could keep pace with sea level during periods of rapid sea-level rise, previous work[2] estimated that MWP-1A occurred between 14.2 kyr ago (ka) and 13.5 ka and had a rsl amplitude of 14–24 m. However, dated samples of the shallow-water coral species (*Acropora palmata*) before 14.2 ka suggest
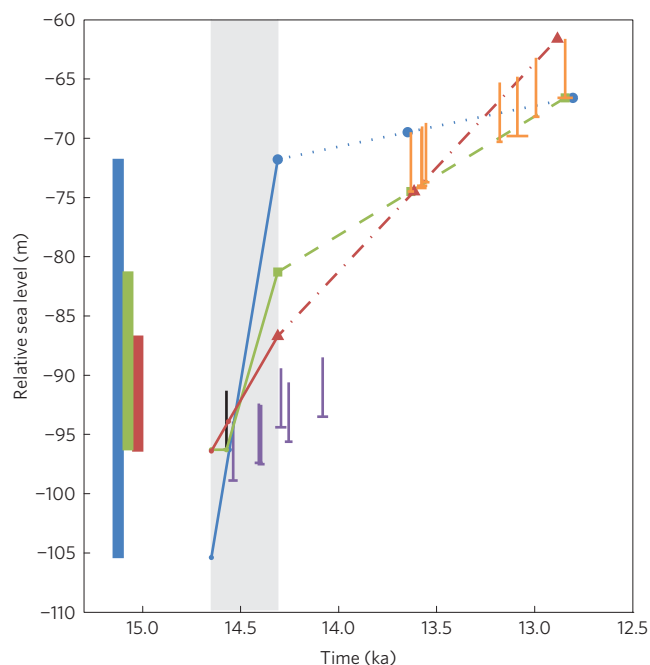

Figure 1 | Illustration of method used to estimate MWP-1A amplitude at Barbados using age and depth information from coral samples. Horizontal bars denote age uncertainties and hard lower bounds. Vertical bars denote depth uncertainties. Purple points are from site 9, orange from site 12, and black from site 15 of Peltier and Fairbanks[2]. Grey box denotes MWP-1A timing based on the Tahitian record of Deschamps and colleagues[1]. A maximum MWP-1A sea-level change is set by the lowest slope that is consistent with the observations within uncertainty of sea level after MWP-1A (blue dotted line), and a minimum sea-level change is set by the steepest consistent slope (red dashed-dotted line). As the first two sample observations plotted (black and leftmost purple index points) are the same age within uncertainty, we took the overlapping depth range and total combined age range for these two index points to define our earliest data constraint and extrapolated back to 14.65 ka, the earliest that MWP-1A could have begun[1], to get the starting depth of MWP-1A. The solid blue and red lines show how the MWP-1A amplitudes were determined from extrapolation. Thick blue and red bars denote the corresponding estimates of maximum and minimum MWP-1A amplitudes. The solid and dashed green lines illustrate the method of Deschamps et al.[1], who did not consider data uncertainty and extrapolated back in time to the first index point shown, rather than 14.65 ka as we have done. The thick green bar shows the MWP-1A amplitude estimated by Deschamps and colleagues[1].

[1]Department of Earth and Environmental Sciences, University of Ottawa, Ottawa, Ontario K1N 6N5, Canada. [2]Department of Earth & Planetary Sciences, Rutgers Energy Institute, and Institute of Earth, Ocean & Atmospheric Sciences, Rutgers University, New Brunswick, New Jersey 08904, USA. [3]College of Earth, Ocean, and Atmospheric Sciences, Oregon State University, Corvallis, Oregon 97331, USA. [4]Department of Geography, Durham University, Durham, County Durham DH1 3LE, UK. *e-mail: gamilne@uottawa.ca
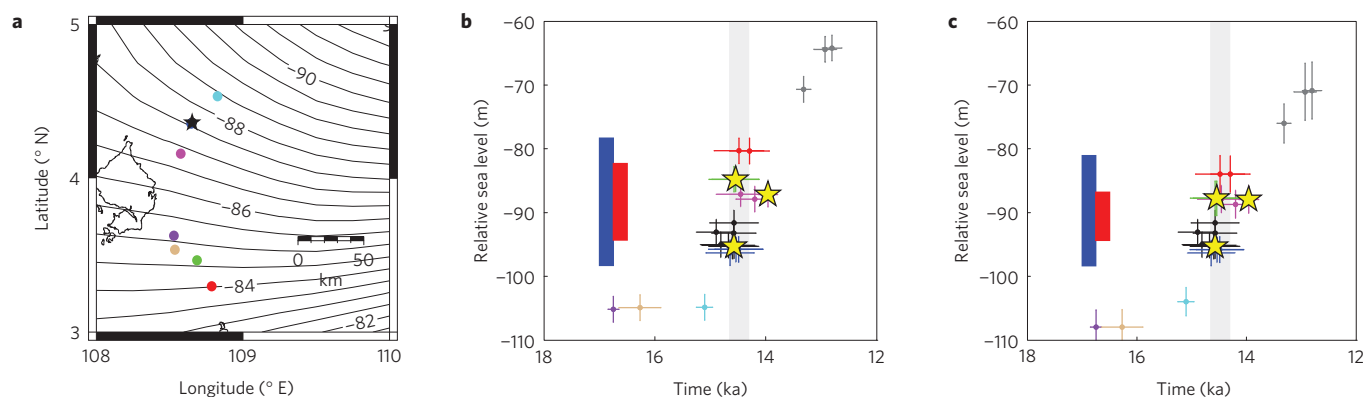
Figure 2 | Relative sea-level reconstructions for the Sunda Shelf and model estimate of sea-level gradient across this region at the time of MWP-1A.
a, Sea-level contour lines across Sunda Shelf are the mean of a model ensemble (see Methods). Black star denotes site 18300, to which all other sites are reduced; site 18299 (cyan dot), site 18301 (dark blue dot; partially hidden by black star), site 18302 (magenta dot), site 18307 (purple dot), site 18308 (red dot), site 18309 (green dot) and site 18310 (tan dot) from the Hanebuth et al.[3] study. **b,c**, Relative sea-level constraints at the Sunda Shelf before (**b**) and after (**c**) the spatial correction is made, with colours corresponding to different core sites as defined in **a** and yellow stars marking in situ samples. Horizontal bars mark age uncertainty. Vertical bars mark depth uncertainty, which includes GIA model uncertainty in **c**. Blue and red bars depict the maximum and minimum local MWP-1A amplitude respectively. Grey box denotes MWP-1A timing[1]. The three youngest sea-level index points (grey) are from core locations outside of the area shown in **a**; these were not used in constraining the amplitude of MWP-1A.

that this interpretation may be incorrect: specifically, the rate of sea-level rise had already increased before 14.2 ka (ref. 11) and the shallow-water corals were already in the process of drowning owing to rapid rates of sea-level rise[7,16]. A recent study of coral records from Tahiti supports the latter interpretation by constraining MWP-1A to have occurred within the period 14.65–14.31 ka (ref. 1), thus defining a maximum duration of 340 years for the event. Adopting 14.31 ka as the end of MWP-1A, Deschamps et al.[1] estimated the Barbados MWP-1A amplitude to be ~15 m (Fig. 1). In this study, we extended this reappraisal by considering the depth and age uncertainties of the Barbados coral record, and arrived at a MWP-1A amplitude range of 9.7–33.6 m at this location (Fig. 1). The maximum estimate is large and could probably be reduced using a more sophisticated approach that considers additional information, such as reef morphology and stratigraphy; however, this is beyond the scope of this study. Furthermore, we note that the upper bound at this site does not play an important role in our final results (see below).

The Sunda Shelf record[3] is defined by rooted mangrove trees, which, like corals, grow in a specific elevation range relative to mean sea level. Fossil mangrove roots were recovered from sediment cores distributed over a relatively large area of the shelf (Fig. 2a). Assuming that all the core sites reflect the same sea-level history suggests that MWP-1A had a rsl amplitude of 12–20 m and occurred at the same time as it did in Tahiti[1,3] (Fig. 2b). There is, however, a considerable sea-level gradient across the region due to water loading associated with flooding of the shelf[17] (Fig. 2a); this gradient influences the estimated MWP-1A amplitude because the core locations are widely separated. Using the GIA sea-level model introduced above with two alternative ice models and 162 combinations of Earth model parameters, we translated the Sunda Shelf observations to their equivalent values at a single location, site 18300 (Fig. 2a, black star; see Methods). The model results indicate that this translation leads to a 2–4 m correction in rsl at sites where samples define the beginning (Fig. 2a, blue dot) and end (Fig. 2a, red dot) of MWP-1A. Correcting for the spatial sea-level gradient yields a MWP-1A amplitude of 7.5–17.3 m (Fig. 2c), which is significantly reduced compared to the original interpretation[3] (Fig. 2b).

The final observations we consider are from Tahiti, which, as described earlier, are from a well-dated high-resolution coral record[1]. A large number of cores were drilled, resulting in a local sea-level record that agrees with a heterogeneous

reef-accretion model[18] and indicates a local MWP-1A amplitude of 12–22 m (ref. 1).

We applied the sea-level fingerprinting technique within a Bayesian statistical framework to assess the likelihood of different MWP-1A source geometries (see Methods). Nine spatial functions were defined to represent ice thickness changes across MWP-1A. Elastic-Earth sea-level fingerprints were computed for each of these and then combined using different weighting coefficients to test a large number of source scenarios (of the order of 10,000) to satisfy statistical requirements. The contribution of viscous Earth deformation due to ice–ocean loading and rotational changes before MWP-1A was included by means of a model correction to the observed MWP-1A amplitudes described above (see Methods and Supplementary Table 1).

The nine spatial functions are based on deglaciation models of the Antarctic ice sheets (AIS; refs 19–21), North American ice sheets (NAIS; refs 12,22,23), Fennoscandian ice sheet (FIS; ref. 24) and Greenland ice sheet (GIS; ref. 25). As the focus of this analysis is the AIS and NAIS, we decomposed these ice complexes into several spatial functions, which are based on common elements from different deglaciation models and so are relatively robust. The Antarctic contribution to MWP-1A is defined using four spatial functions, corresponding to Wilkes Land, the Weddell Sea, the Ross Sea and the Antarctic Peninsula (Supplementary Fig. 2). The North American contribution is defined using three spatial functions based on recent modelling results for this ice complex[11,22,23] (Supplementary Fig. 3a–c). A single spatial function is defined for each of the FIS and GIS, because the contribution of these ice sheets to MWP-1A was relatively minor and is less debated[11]. Their spatial functions are taken directly from recent reconstructions[24,25] across the appropriate time window (Supplementary Fig. 3d,e).

For each spatial function, except that of the NAIS saddle collapse (Supplementary Fig. 3c), the prior probability distribution of melt amplitude was taken as uniformly distributed between zero and twice the maximum melt contribution suggested in the source literature (Supplementary Table 3). For the saddle-collapse scenario, the upper bound of the amplitude prior was set equal to the estimated MWP-1A amplitude (15 m sea-level equivalent (ref. 1). The contributions from the AIS as a whole, the NAIS as a whole, and the FIS and GIS were treated as uncorrelated. Contributions from individual components of the AIS and of the NAIS were treated as uncorrelated before conditioning on the total AIS or NAIS contribution.
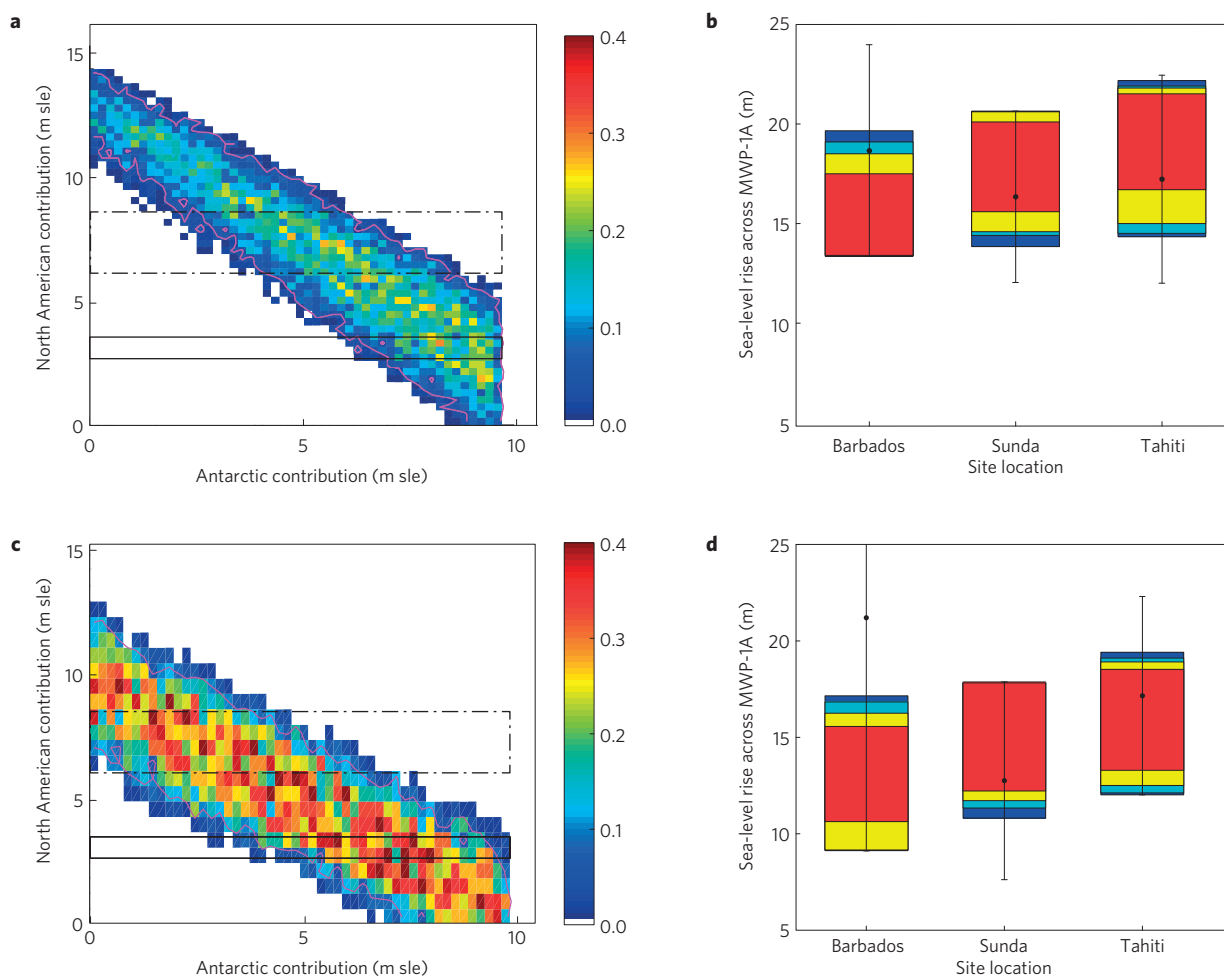
Figure 3 | Posterior distribution of NAIS and AIS sea-level contributions conditioned on far-field rsl reconstructions. a,c, Results for previously published far-field MWP-1A amplitude estimates[1-3] (**a**) and for our revised amplitude estimates (**c**), with solution density (m^{-2}) indicated by the colour scale. The magenta contour indicates the central 95% credible range. The black outlines indicate two recent estimates of the NAIS contribution to MWP-1A based on near-field evidence: 2.8–3.7 m sle (solid line; ref. 11) and 6.4–9.0 m sle (dashed–dotted line; ref. 12). **b,d**, MWP-1A amplitudes and uncertainties at each of the considered far-field sites (thin vertical bars) corresponding to **a** and **c**, respectively, with coloured bars showing the local MWP-1A amplitudes produced by scenarios that satisfy all far-field constraints. Cyan, yellow and red bars show the 99%, 95% and 67% credible intervals, respectively. The full range (minimum to maximum) is represented by the dark blue bars. Note that the model-corrected upper bound of MWP-1A amplitude at Barbados (33.6 m) is not visible.

We randomly sampled 40,000 individual MWP-1A source scenarios from the prior probability distribution (Supplementary Table 3 and Supplementary Figs 4 and 5). The likelihood of each scenario was then determined by comparing the calculated rsl rise to the model-corrected observations (Supplementary Tables 1 and 2). Figure 3 shows the joint posterior probability distribution for the NAIS and AIS contributions when the original (Fig. 3a) and our revised (Fig. 3c) estimates of MWP-1A amplitude at Barbados and Sunda Shelf are adopted (the Tahiti amplitude range is the same in each case, 12–22.4 m (model-corrected range from ref. 1)). As expected, the NAIS and AIS contributions are negatively correlated: as the contribution from one increases, less mass is required from the other. Posterior contribution estimates (95% probability) for the FIS and GIS are 0 to 2 m and 0 to 0.4 m sle, respectively (Table 1). These values are the same as the prior ranges (0–2.2 m and 0–0.4 m sle), indicating that the far-field data considered do not constrain the contribution of these ice sheets to MWP-1A.

Two recent studies[11,12] considered near-field evidence to constrain the NAIS MWP-1A contribution to either 2.8–3.7 m or 6.4–9.0 m sle (solid[11] and dashed–dotted[12] black boxes in Fig. 3a,c;

the values provided in these studies, 6.7–8.7 m over 800 years (ref. 11) and 9.4–13.2 m over 500 years (ref. 12), were scaled linearly to determine amplitudes for the 340-year interval from Tahiti[1]). These estimates are based on both field and model constraints, but apply different approaches to arrive at the ranges given. Rather than argue for the veracity of one over the other, we consider each to be equally plausible.

Jointly conditioning the prior probability distribution on these alternative near-field constraints and the model-corrected MWP-1A original amplitudes inferred at Barbados[2] and Sunda Shelf[3], as well as the more recent Tahiti constraint[1], indicates a 95% credible AIS contribution of either 5.9–10.1 m (ref. 11) or 2.1–9.1 m (ref. 12) sle (magenta curves in Fig. 3a), corresponding to a global mean sea-level rise of 11.2–16.1 m or 11.8–16.7 m, respectively. In comparison, using our revised far-field estimates leads to plausible MWP-1A source scenarios (Fig. 3c) with AIS contributions of 4.1–10.0 m (ref. 11) or 0–6.9 m (ref. 12) sle, and an estimated global mean sea-level rise of 9.3–14.6 m or 8.6–14.4 m sle, respectively (see Table 1 for a summary of results).

A recent fingerprinting analysis[26] to evaluate the plausibility of a large (~10 m) NAIS contribution to MWP-1A through a

Table 1 | Posterior estimates on MWP-1A source partitioning.

Ice sheet(s)	Prior distribution (m)	Given NAIS constraints of 2.8–3.7 m (ref. 11)		Given NAIS constraints of 6.4–9.0 m (ref. 12)	
		Original far-field constraints (m)	Revised far-field constraints (m)	Original far-field constraints (m)	Revised far-field constraints (m)
Antarctic	0–10.2	5.9–10.1	4.1–10.0	2.1–9.1	0–6.9
North American	0–32.4	2.8–3.7	2.8–3.7	6.4–9.0	6.4–9.0
Fennoscandian	0–2.2	0–2.2	0–2.2	0–2.2	0–2.2
Greenland	0–0.4	0–0.4	0–0.4	0–0.4	0–0.4
Total	0–45.2	11.2–16.1	9.3–14.6	11.8–16.7	8.6–14.4

Quoted results are 95% credible intervals. Ice volumes given as metres of sea-level equivalent calculated using the present-day ocean area.

saddle collapse between the Cordilleran and Laurentide ice sheets demonstrated that the far-field constraints (different from those considered here for Barbados and Tahiti) are compatible with such a scenario. This study also concluded that the observations do not exclude the case of a dominant AIS contribution. The results in Fig. 3c are consistent with the results of ref. 26.

The 95% credible estimates of the local MWP-1A rsl amplitudes are 9.1–16.3 m at Barbados, 11.7–17.9 m at Sunda Shelf, and 12.5–19.0 m at Tahiti (red and yellow ranges in Fig. 3d). The results in Fig. 3d indicate that the observed lower bound on MWP-1A amplitude at Barbados and Tahiti and upper bound at Sunda Shelf provide the primary constraints on the possible solution space. Therefore, new evidence from these locations that improves on the observational precision of these specific aspects of the local MWP-1A amplitude would reduce the posterior uncertainties. As an example, increasing the value of the lower bound at Barbados leads to estimates with a larger AIS contribution (Supplementary Fig. 6). Note, however, that a relatively large change in this value is required to markedly influence the results.

Our analysis conclusively demonstrates that, when data and model uncertainties are carefully accounted for, the presently available far-field rsl reconstructions do not provide tightly bounded constraints on MWP-1A partitioning: specifically, the 95% credible AIS contribution to MWP-1A is 0–10.0 m sle when recent estimates of the NAIS contribution are considered[11,12]. Accordingly, our reassessment indicates that a significant AIS contribution may not be required, thus potentially reconciling the apparent inconsistency between near-field[10] and far-field evidence. At the same time, however, our results suggest that a dominant AIS contribution remains equally plausible. We note that any future improvements on the total NAIS contribution can be directly applied to our AIS–NAIS partitioning diagram (Fig. 3c) and anticipate that the approach taken here will provide the means to further constrain the source regions of MWP-1A as more geologic evidence becomes available. At present, uncertainty in the source distribution of MWP-1A remains a primary limitation in our understanding of the causes and consequences of this extreme event.

Methods

Methods and any associated references are available in the online version of the paper.

References

1. Deschamps, P. et al. Ice-sheet collapse and sea-level rise at the Bølling warming 14,600 years ago. Nature 483, 559–564 (2012).
2. Peltier, W. R. & Fairbanks, R. G. Global glacial ice volume and last glacial maximum duration from an extended Barbados sea level record. Quat. Sci. Rev. 25, 3322–3337 (2006).
3. Hanebuth, T., Stattegger, K. & Grootes, P. M. Rapid flooding of the Sunda shelf: A late-glacial sea-level record. Science 288, 1033–1035 (2000).
4. Golledge, N. R. et al. Antarctic contribution to meltwater pulse 1A from reduced Southern Ocean overturning. Nature Commun. 5, 5107 (2014).
5. Menviel, L., Timmermann, A., Timm, O. E. & Mouchet, A. Deconstructing the Last Glacial termination: The role of millennial and orbital-scale forcings. Quat. Sci. Rev. 30, 1155–1172 (2011).
6. Stouffer, R. J., Seidov, D. & Haupt, B. J. Climate response to external sources of freshwater: North Atlantic versus the Southern Ocean. J. Clim. 20, 436–448 (2007).
7. Weaver, A. J., Saenko, O. A., Clark, P. U. & Mitrovica, J. X. Meltwater pulse 1A from Antarctica as a trigger of the Bølling–Allerød warm interval. Science 299, 1709–1713 (2003).
8. Clark, P. U., Mitrovica, J. X., Milne, G. A. & Tamisiea, M. E. Sea-level fingerprinting as a direct test for the source of global meltwater pulse 1A. Science 295, 2438–2441 (2002).
9. Bassett, S. E., Milne, G. A., Mitrovica, J. X. & Clark, P. U. Ice sheet and solid Earth influences on far-field sea-level histories. Science 309, 925–928 (2005).
10. Bentley, M. J. et al. A community-based geological reconstruction of Antarctic Ice Sheet deglaciation since the Last Glacial Maximum. Quat. Sci. Rev. 100, 1–9 (2014).
11. Carlson, A. E. & Clark, P. U. Ice sheet sources of sea level rise and freshwater discharge during the last deglaciation. Rev. Geophys. 50, RG4007 (2012).
12. Tarasov, L., Dyke, A. S., Neal, R. M. & Peltier, W. R. A data-calibrated distribution of deglacial chronologies for the North American ice complex from glaciological modelling. Earth Planet. Sci. Lett. 315–316, 30–40 (2012).
13. Mitrovica, J. X., Tamisiea, M. E., Davis, J. L. & Milne, G. A. Recent mass balance of polar ice sheets inferred from patterns of global sea-level change. Nature 409, 1026–1029 (2001).
14. Fairbanks, R. G. A 17,000-year glacio-eustatic sea level record: Influence of glacial melting rates on the Younger Dryas event and deep-ocean circulation. Nature 342, 637–642 (1989).
15. Bard, E., Hamelin, B. & Fairbanks, R. G. U–Th ages obtained by mass spectrometry in corals from Barbados: Sea level during the past 130,000 years. Nature 346, 456–458 (1990).
16. Neumann, A. C. & McIntyre, I. G. Proc. 5th Int. Coral Reef Cong. Tahiti Vol. 3 105–110 (WorldFish, 1985).
17. Lambeck, K., Yokoyama, Y. & Purcell, T. Into and out of the Last Glacial Maximum: Sea-level change during Oxygen Isotope Stages 3 and 2. Quat. Sci. Rev. 21, 343–360 (2002).
18. Blanchon, P. & Blakeway, D. Are catch-up reefs and artifact of coring? Sedimentology 50, 1271–1282 (2003).
19. Briggs, R. D., Pollard, D. & Tarasov, L. A data-constrained large ensemble analysis of Antarctic evolution since the Eemian. Quat. Sci. Rev. 103, 91–115 (2014).
20. Gomez, N., Pollard, D. & Mitrovica, J. X. A 3-D coupled ice sheet-sea level model applied to Antarctica through the last 40 ky. Earth Planet. Sci. Lett. 384, 88–99 (2013).
21. Whitehouse, P. L., Bentley, M. J. & Le Brocq, A. M. A deglacial model for Antarctica: Geological constraints and glaciological modelling as a basis for a new model of Antarctic glacial isostatic adjustment. Quat. Sci. Rev. 32, 1–24 (2012).
22. Carlson, A. E. et al. Modeling the surface mass-balance response of the Laurentide Ice Sheet to Bølling warming and its contribution to Meltwater Pulse 1A. Earth Planet. Sci. Lett. 315–316, 24–29 (2012).
23. Gregoire, L. J., Payne, A. J. & Valdes, P. J. Deglacial rapid sea-level rises caused by ice-sheet saddle collapses. Nature 487, 219–222 (2012).
24. Lambeck, K., Smither, C. & Johnston, P. Sea-level change, glacial rebound and mantle viscosity for northern Europe. Geophys. J. Int. 134, 102–144 (1998).

25. Simpson, M. J. R., Milne, G. A., Huybrechts, P. & Long, A. J. Calibrating a glaciological model of the Greenland ice sheet from the Last Glacial Maximum to present-day using field observations of relative sea level and ice extent. *Quat. Sci. Rev.* **28,** 1631–1657 (2009).

26. Gomez, N., Gregoire, L. J., Mitrovica, J. X. & Payne, A. J. Laurentide-Cordilleran ice sheet saddle collapse as a contribution to meltwater pulse 1A. *Geophys. Res. Lett.* **42,** 3954–3962 (2015).

Author contributions

J.L. performed the research and led the writing of the manuscript. G.A.M., R.E.K., P.U.C. and I.S. advised J.L. in performing the research and contributed to the writing of the manuscript.

Additional information

Supplementary information is available in the online version of the paper. Reprints and permissions information is available online at www.nature.com/reprints. Correspondence and requests for materials should be addressed to G.A.M.

Competing financial interests

The authors declare no competing financial interests.

Methods

Sea-level model. The glacial isostatic adjustment (GIA) model adopted in this study computes sea-level changes due to solid Earth deformation and gravity changes associated with the redistribution of ice and water on the Earth's surface[27–29]. In addition to the ice–ocean loading, the model also includes the influence of changes in Earth rotation due to GIA (refs 30–32), as this can contribute significantly to the sea-level response, particularly during rapid and large events such as Meltwater Pulse 1A (MWP-1A; refs 8,26,33).

The two primary inputs to the model are a spacetime reconstruction of grounded ice thickness and a model of Earth sub-surface density and rheology structure. Different ice models are applied in this study, and are defined and described where appropriate. The adopted Earth model is spherically symmetric and so includes only changes in parameters with depth. The elastic and density depth profiles are taken from a seismic model[34] and are defined with a depth resolution of 10–25 km. These profiles were not varied in this analysis. The viscous structure is less precisely known and so a large range of parameters was considered (details below where appropriate). Given the relatively large uncertainty in this model aspect, the depth parameterization of the viscosity profile was considerably lower resolution compared to that for the elastic and density changes. Following a number of previous GIA analyses, we define an outer shell with very high viscosity (10^{43} Pa s) to simulate an elastic lithosphere; the thickness of this outer shell is varied in the modelling. We define an 'upper mantle' region from the base of the model lithosphere to 670 km depth and a 'lower mantle' region from 670 km to the core–mantle boundary. Viscosity is defined to be uniform in these two regions.

MWP-1A amplitude at the Sunda Shelf. Given the relatively large spatial spread in the locations where relative sea level (rsl) was reconstructed on the Sunda Shelf, it is necessary to reduce the observations to a single locality to accurately determine the local MWP-1A amplitude. We applied the model described in the previous section for this purpose and computed rsl in the region for a total of 324 parameter sets comprising two ice models (ICE5G; ref. 35 and that of Bassett *et al.*[9]) and 162 Earth viscosity models (lithosphere thickness of 71, 96 and 120 km; upper mantle viscosity of 0.1, 0.2, 0.3, 0.5, 0.8 and 1×10^{21} Pa s; and lower mantle viscosity of 1, 2, 3, 5, 8, 10, 20, 30 and 50×10^{21} Pa s). We used the mean difference between the sea level at each core location and that at core site 18300 to define a spatial correction for each rsl data point, calibrated with IntCal13 (ref. 36) around the MWP-1A period (Fig. 2a, main text). The uncertainty in the model correction was taken to be the spread in results produced by the parameter ranges defined above. By reducing the rsl index points to a single location (core site 18300: 4.3630° N, 108.6536° E), we found a revised MWP-1A amplitude of 7.5–17.3 m, compared with 12–20 m for the uncorrected data.

We are confident that the range in model parameters considered provides a conservative estimate of the model uncertainty in the spatial correction applied. Given that the primary contributor to the spatial rsl gradient in this region is ocean loading, the sensitivity of the results to the ice history is largely through the time variation in the global ice volume (or sea-level equivalent, sle) rather than differences in the spatial distribution of ice through time. Both of the ice models adopted have been calibrated to fit far-field rsl observations for considerably different Earth viscosity models, leading to significant differences in their respective sle curves[9,35]. Furthermore, the two models are based on contrasting source scenarios for MWP-1A (one[35] solely northern and the other[9] dominantly southern). Therefore, we believe that these two models probably bound the uncertainty associated with the aspect of the ice model that influences the modelled ocean loading. With regard to the Earth model viscosity structure, the parameter ranges adopted probably overestimate the uncertainty in this model input.

Contribution of viscous Earth deformation to the sea-level fingerprints. Spatial patterns of rsl change associated with changes in land ice are governed by the geographic distribution of ice mass changes and the associated deformational response of the solid Earth[37]. Over relatively short timescales (a few centuries), the contribution of viscous Earth deformation to the pattern of rsl change is relatively small compared to changes over longer time periods (multi-millennial to deglacial) that have been more commonly considered in GIA modelling studies. Thus, a primary benefit of short-timescale problems such as MWP-1A is that sensitivity to Earth viscosity is relatively low[8,26], and so the considerable uncertainty in this model parameter is less influential on the results. However, viscous deformation can contribute as much as a metre or so to the computed sea-level fingerprints[8,26], and so we consider its impact by estimating and then removing it from the far-field rsl constraints of local MWP-1A amplitude.

There are two components of viscous solid Earth deformation that contribute to the spatial pattern (or fingerprint) of rsl change during MWP-1A: that associated with ice–ocean loading and rotational changes before the event and that due to these changes during the event. We consider only the former, as computing the viscous deformation associated with the large number of source scenarios (tens of thousands) required to ensure our results were statistically robust is computationally prohibitive.

The magnitude of the pre-MWP-1A viscous 'overprint' depends on a number of factors, including the amplitude and timing of the loading and rotational changes before MWP-1A, the viscosity structure of the Earth and the duration of MWP-1A (ref. 26) (the longer the duration, the larger the viscous contribution will be). We computed the viscous response due to loading before MWP-1A at all three sites using the suite of ice and Earth model parameters described in the previous section (324 model runs in total) by running the full time history of the ice model: from the end of the last interglacial up to 14.5 ka. The model was then run for an additional time step of 500 years, with no further loading or rotational changes, to determine the viscous contribution over the period 14.5 to 14.0 ka. Given that the viscous signal is approximately linear over this period[26], we scaled the results to be representative of a 340-year interval, as adopted elsewhere in this analysis. Our results (Supplementary Fig. 1) agree in sign and are similar in amplitude to those in ref. 26 (see their Fig. 3). However, because we neglected the viscous deformation during MWP-1A, the mean of our model spread is less than the values presented in ref. 26.

The pre-MWP-1A viscous signal shown in Supplementary Fig. 1 was incorporated into our final results (Fig. 3) by considering the full range of the model spread. The model spread was combined directly with the observed values to produce a conservative estimate of the uncertainty associated with the pre-MWP-1A viscous contribution. The raw and model-corrected MWP-1A amplitudes are given in Supplementary Table 1. To test the impact of pre-MWP-1A viscous deformation on our final results, we computed the posterior probability estimates without applying this model correction (that is, ignoring all viscous effects) (Supplementary Table 2). The results show that the estimated AIS contribution is affected, but those for the FIS and GIS are not. The differences in the AIS 95%-credible ranges, with and without the viscous correction, are relatively small and depend on the adopted range for the NAIS contribution.

Melt source geometries. To compute rsl fingerprints associated with ice sheet changes during MWP-1A, it is necessary to define the melt source geometries to be tested. As described in the main text, we did this by specifying nine spatial functions identified from a number of recent ice model reconstructions. For Antarctica and North America, specific source regions within these ice complexes were defined (Supplementary Figs 2 and 3a–c, respectively). For these regions, more than one model reconstruction was considered (see main text) so as to determine source regions that are compatible with multiple studies, and thus more robust. In contrast, the melt distributions for Fennoscandia and Greenland were taken directly from single studies (see main text; Supplementary Fig. 3d,e), given that their contribution to MWP-1A is relatively minor and less debated[11].

We note that the spatial functions defined in Supplementary Figs 2 and 3 have relatively crude spatial fidelity as they were not intended to accurately define the changes in ice distribution during MWP-1A. Rather, they were intended to provide only an approximate representation of these changes for each region. Although our final results (Fig. 3, main text) indicate that the far-field rsl constraints show a clear sensitivity to the partitioning of mass loss between the AIS and NAIS, their sensitivity to the partitioning of mass loss within these regions is much less pronounced, particularly for Antarctica. Therefore, we believe that the spatial fidelity of the AIS and NAIS source functions is more than adequate, given the limited geographic distribution and precision of the rsl data considered.

The nine functions defining ice changes during MWP-1A were used as input to the GIA sea-level model to compute the rsl rise at each of the three far-field sites for the case of an elastic-Earth rheology. The computed rise at each site was normalized by the volume of ice loss (in metres sle) to define a 'fingerprint' for each melt source.

Statistical methodology. We quantify the Bayesian probability of different alternative source region contributions to MWP-1A. If **H** is a particular set of ice sheet contributions, **F** the far-field observational constraints, and **N** the near-field observational constraints, then by Bayes' theorem,

$$P(\mathbf{H}\,|\,\mathbf{F},\mathbf{N}) \sim P(\mathbf{F},\mathbf{N}\,|\,\mathbf{H})P(\mathbf{H}) \qquad (1)$$

To estimate the posterior probability distribution $P(\mathbf{H}\,|\,\mathbf{F},\mathbf{N})$, we took 40,000 maximin Latin hypercube samples from the prior probability distribution $P(\mathbf{H})$, which is described below, and weight each sample by its likelihood, $P(\mathbf{F},\mathbf{N}\,|\,\mathbf{H})$. We assume that the far-field observations have uniform likelihoods in terms of rsl (which is a linear transformation of **H**, generated using the spatial functions described above). In particular, we assume that Barbados, Sunda Shelf and Tahiti have likelihoods that are, respectively, uniform between 9.0–33.6 m, 7.5–17.9 m and 12.0–22.4 m rsl (Supplementary Table 1). We further assume that the near-field observations have uniform likelihoods in terms of ice volume; thus, they serve simply to truncate the posterior distribution calculated by conditioning on far-field distributions. As a result of the uniform likelihoods, each sample from $P(\mathbf{H})$ has a relative weight of either zero or $1/n$, where n is the total number of samples with non-zero likelihoods.

The priors for the individual source regions are shown in Supplementary Table 3. To help account for differences in the interpretation of near-field data[11]

and to remain consistent with the conservative nature of this analysis, the upper bound to the uniform prior for eight of the nine source regions was set equal to twice that indicated in the source literature. For the region that represents the saddle-collapse signal[12,23] (Supplementary Fig. 3c), the upper bound for the uniform prior was set equal to 15 m sle (Supplementary Table 3). For each component source region in the AIS and NAIS, we used a uniform prior that is conditioned on the uniform prior for the ice sheet as a whole; these were sampled by first sampling from the prior for the ice sheet as a whole, then randomly dividing the ice sheet into sections, and rejecting those divisions incompatible with the uniform priors for the individual source regions.

Supplementary Fig. 4 shows the sampling density for the NAIS versus the AIS, as well as histograms indicating the number of samples for a given total contribution from each of the four source regions. From the sampled total contribution of the AIS and NAIS, contributions from the sub-sectors were sampled until all sub-sector constraints compatible with the specified total AIS/NAIS contribution were satisfied. Supplementary Fig. 5 provides histograms of the number of times a given sub-sector contribution was sampled.

Code availability. The code used for the statistical analysis is available on request.

References

27. Farrell, W. E. & Clark, J. A. On postglacial sea-level. *Geophys. J. R. Astron. Soc.* **46,** 647–667 (1976).
28. Mitrovica, J. X. & Milne, G. A. On post-glacial sea level-I. General theory. *Geophys. J. Int.* **154,** 253–267 (2003).
29. Kendall, R., Mitrovica, J. X. & Milne, G. A. On post-glacial sea level-II. Numerical formulation and comparative results on spherically symmetric models. *Geophys. J. Int.* **161,** 679–706 (2005).
30. Sabadini, R., Yuen, D. A. & Boschi, E. Polar wander and the forced responses of a rotating, multi-layered, viscoelastic planet. *J. Geophys. Res.* **87,** 2885–2903 (1982).
31. Milne, G. A. & Mitrovica, J. X. Postglacial sea-level change on a rotating Earth. *Geophys. J. Int.* **133,** 1–19 (1998).
32. Mitrovica, J. X., Wahr, J., Matsuyama, I. & Paulson, A. The rotational stability of an ice-age Earth. *Geophys. J. Int.* **161,** 491–506 (2005).
33. Mitrovica, J. X. *et al.* On the robustness of predictions of sea level fingerprints. *Geophys. J. Int.* **187,** 729–742 (2011).
34. Dziewonski, A. M. & Anderson, D. L. Preliminary Reference Earth Model (PREM). *Phys. Earth Planet. Inter.* **25,** 297–356 (1981).
35. Peltier, W. R. Global glacial isostasy and the surface of the ice-age Earth: The ICE-5G (VM2) model and GRACE. *Annu. Rev. Earth Planet Sci.* **32,** 111–149 (2004).
36. Reimer, P. J. *et al.* IntCal13 and Marine13 radiocarbon age calibration curves 0–50,000 years cal BP. *Radiocarbon* **55,** 1869–1887 (2013).
37. Clark, J. A., Farrell, W. E. & Peltier, W. R. Global changes in postglacial sea level: A numerical calculation. *Quat. Res.* **9,** 265–287 (1978).